Hybrid acceleration of compact ion bunches by few-cycle laser pulses in gas jets of two atomic species

Zs. Lécz,[1,*] R. Polanek,[1] A. Andreev,[1,†] A. Sharma,[1] D. Papp,[1] N. Hafz,[1,2,‡] and C. Kamperidis[1]
[1]*ELI-ALPS, ELI-HU Non-Profit Ltd. Wolfgang Sadner str 3., 6728 Szeged, Hungary*
[2]*Doctoral School of Physics, Faculty of Science and Informatics, University of Szeged, Dóm tér 9, Szeged 6720, Hungary*

(Received 4 October 2022; accepted 18 May 2023; published 16 June 2023)

Extreme states of matter that exist for a short time need probing with compact proton sources. Here, the generation of a compact MeV-energy proton source from few-cycle laser pulse interaction with narrow gas-jet target is demonstrated numerically. We realize such proton source by incorporating a gas mixture which is optimal for generation of quasimonoenergetic proton bunches. In the presented laser-plasma interaction we identify the ion acceleration from magnetic vortex, charge separation, and collisionless shock wave. The proposed particle source is excellent for applications where moderate-energy proton bunches are used at high repetition rate. We prove the applicability of this scheme for generating a pulsed spherical neutron burst with ∼100 ps duration.

DOI: 10.1103/PhysRevResearch.5.023169

I. INTRODUCTION

Energetic proton beams are routinely generated in laser-driven ion acceleration experiments having a bunch length on the order of several picoseconds at the source [1], which increases during propagation in vacuum. The bunch elongation over time is dictated by the energy spread within the accelerated ion bunch, therefore, quasimonoenergetic and short bunches are desired for efficient beam transport stages. On the other hand, shorter proton bunches would allow an *in situ* diagnostics of fast evolving plasma fields, on the timescale of 100 fs. The first employment of laser-generated proton bunches [2–4] to capture the field dynamics in laser-foil interaction has motivated further research to enhance the spatial and temporal resolution of the proton imaging [5,6]. However, by using solid-density foil targets, the temporal resolution has been limited to the picosecond level due to the thermal energy distribution of the protons, which seems to be an intrinsic feature of the acceleration scheme [1,7]. Another important application of energetic protons is the generation of fast neutrons to investigate the internal structure of solid density materials [8,9]. Laser-driven neutron sources [10–13] provide an alternative way to access energetic neutrons for imaging purposes. The generation of directed neutron beams is more difficult because it requires high-energy (>10 MeV) primary particles (ions), while the generation of isotropic neutron burst is relatively straightforward. The duration of the neutron emission is strictly defined by the length of the ion bunch, therefore, fast imaging on the subnanosecond timescale remains challenging. By including moderator stages [14] these neutrons become a valuable source for cancer therapy [15].

Although in PW-class laser-foil experiments the maximum proton energy approaches the 100-MeV level [16,17], in several applications [18–20] small divergence and small source size of the beam are more important and moderate ion energies (MeV level) are desired to be delivered at a high repetition rate. Such proton beams can be produced from solid foil targets as well [21], but several issues with the target replacement are not resolved yet and typically an energy selection procedure is needed in order to reduce the spectral width [22]. Significant achievements have been reported from experiments using liquid targets, which would also allow operation at high repetition rate, but the measured proton beam divergence and energy spread was relatively large [23,24]. Therefore, an alternative way of ion acceleration becomes more demanded, where higher control on phase-space distribution at the source is feasible.

On the other hand, laser-driven ion and proton acceleration in gas-phase targets has attracted a great attention in recent years due to its potential deployment as a source of energetic protons operating at high repetition rates with small debris damaging the surroundings [25–33]. Moreover, the proton energy spread can be reduced significantly [31–33], which is an important step towards generating high-quality and short proton bunches. In those recent experiments, using underdense plasma, energetic ions were detected in a direction nearly perpendicular to the laser axis [25–27] and in the laser propagation direction [28–30] by using 1-μm wavelength lasers and by using CO_2 lasers with 10-μm wavelength [31–33]. In all of these experiments the pulse energy was well above 1 J. For the acceleration in the radial direction the Coulomb explosion of the ion channel, and the consequent shock formation, is responsible and takes place predominantly deep inside the gas jet, where the laser-to-electron energy conversion efficiency is the highest.

*zsolt.lecz@eli-alps.hu
†Present address: Max-Born Institute for Nonlinear Optics, Berlin 12489, Germany.
‡nasr.hafiz@eli-alps.hu

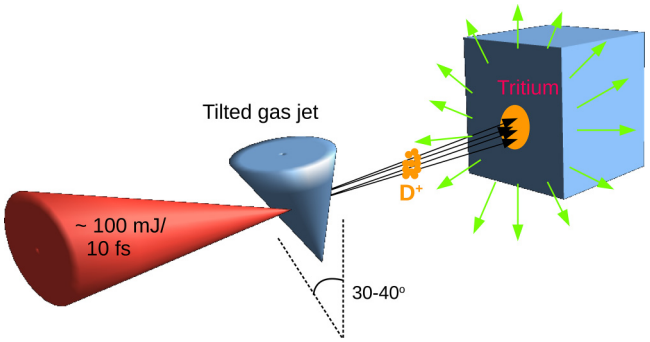

FIG. 1. A proposed experimental scheme for the generation of a narrow energy-spread ultrashort ion (deuteron) bunches and their applicability to the production of ultrafast neutron bursts. A few-cycle laser pulse is focused onto a gas jet, which is tilted towards the incident laser pulse.

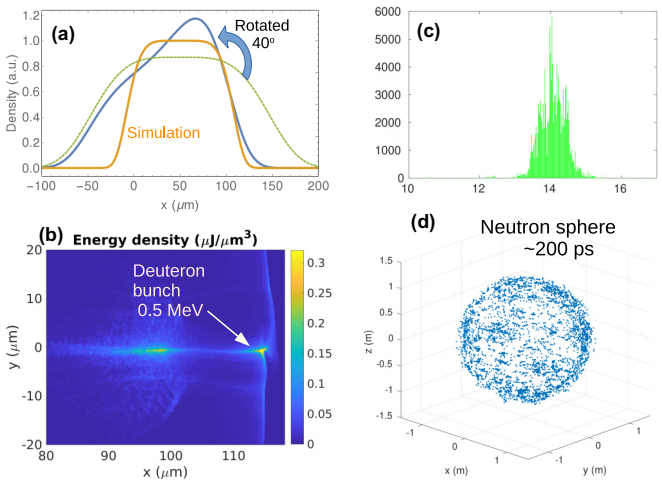

FIG. 2. The on-axis density profile in the down ramp (a) seen by the laser pulse at the exit side is much steeper when the gas jet is tilted (see text for details). The energy density of the ion bunch is shown in (b), which shows a very narrow spatial extension, thus the accelerated bunch is very compact. The energy spectrum of the ion bunch is shown in Fig. 5(c). This short ion bunch is capable of producing a 14.1-MeV (c) neutron burst (d) upon the interaction with a tritium-rich bulk target. The fast neutron bunch resembles a spherical shell (20 ns after the interaction) with a bunch length of the order of 200 ps.

One criterion for observing confined energetic ions in the forward direction is that the pump depletion length must be much longer than the width of the gas jet. Novel technology allows the achievement of such condition even in the case of few-cycle laser pulses [34,35]. Another criterion for reaching MeV energy level of light ions is the high electron density in the target, which is achievable simply by mixing, for instance, the hydrogen gas with a heavier gas, such as oxygen or neon. In the case of 10-fs laser pulse duration the required electron density of the plasma is around 10^{20} cm^{-3}, which is reachable if the oxygen density reaches $\approx 10^{19}$ cm^{-3} in a mixture, where the hydrogen density is around 5×10^{18} cm^{-3}. In this area of near-critical-density plasma, the electron density is around 10% of the critical density, $n_e = 0.1 n_c$ ($n_c = \omega_0^2 m_e \epsilon_0 / e^2$, where ω_0 is the laser frequency, ϵ_0 is the vacuum permittivity, m_e, e are the electron mass and charge, respectively), and the laser absorption is highly efficient.

Here we present a robust method to generate sub-MeV proton (and deuteron) bunches with a very small phase-space volume by using ultrashort laser pulses, having only 10 s of mJ energy, and a density tailored gas jet where two gases are mixed. The electron density profile at the exit side of the gas jet is very important for generating ion bunches compressed in phase space. A steeper profile is required in order to avoid wave breaking of the ion solitary wave launched by the magnetic vortex in the decaying density profile [36]. One way for producing such a sufficiently large density gradient is tilting the gas-jet nozzle by 30°–40° with respect to the axis perpendicular to the laser propagation direction (see Fig. 1). We consider the rotation of a super-Gaussian density profile shown by the dashed green curve in Fig. 2(a), which can be produced by a supersonic gas jet [37]. For a tilting angle of 40° one obtains a profile presented by the blue line in Fig. 2(a), which gives a density gradient very similar to what is used in our simulations [yellow line in Fig. 1(a)]. Such steepness in the plasma distribution can be obtained with density shocks as well, which are achieved by inserting a blade in the gas flow [34,38]. The applicability of the scheme towards the generation of ultrafast 14.1-MeV neutron bursts via the $D(T, n)$He exoergic reaction is also confirmed via Monte Carlo simulations (see Fig. 2).

II. NUMERICAL SETUP

The laser pulse intensity envelope is 8 fs long and 5 μm wide [full width at half-maximum (FWHM)], with Gaussian spatial and temporal profiles, having a peak intensity of 5×10^{19} W/cm^2, thus it contains approximately 60 mJ energy. The laser electric field is polarized along the z direction and it is focused to $x = 0$. In order to accurately model and investigate the acceleration mechanism, three-dimensional (3D) simulations are necessary because of two reasons: (i) in two dimensions (2D) the pulse energy depletion is much smaller than in reality, which results in overestimated efficiency of acceleration and (ii) in 2D the transversal expansion of the fields is linear, while in reality (or in 3D) the energy density decreases as $\sim 1/r^2$, where r is the distance from the axis of symmetry. Consequently, the field gradients in the radial direction can differ significantly in 2D and 3D geometries. In our simulations a static three-dimensional box is used which is 200 μm long (in the x direction) and 100 μm wide in the lateral directions (y and z). This volume is resolved by $4000 \times 500 \times 500$ grid points. The plasma wavelength is close to the laser pulse length, which is around 3.5 μm, therefore, it is well resolved in all directions. Moreover, the laser wavelength is also resolved by 16 points in the x direction.

The target consists of a mixture of oxygen and hydrogen. Both atom species are ionized and further field ionization of O^{5+} is included in the simulation. In this way at 6+ average charge state of oxygen the resultant electron density is nearly $n_e \approx 10^{20}$ cm^{-3}. In each grid cell two ion macroparticles, one oxygen and one hydrogen, and one electron macroparticle are placed initially. The macroparticles have variable weights, which is very important to resolve the density profile near the

edge of the gas jet. The minimum value of the macroparticle weight is 1, which means that the difference between the weights at the center and at the end of the gas target is roughly a factor of 10^4. Later more electrons appear due to field ionization and the number of ions in one Debye sphere (with radius of ≈0.5 μm) is on the order of 10^4. The transversal boundaries are open for electromagnetic fields and reflecting for particles.

The gas-density profile in the case of a symmetric Laval nozzle [37] is well approximated by the function $n \sim \exp[-(x-x_0)^p/\sigma^p]$, where x_0 is the center of the gas jet along the laser propagation axis and σ defines the width of the target. In the case of the green line in Fig. 2(a) the parameters are $\sigma = 104$ μm and $p = 4$, which are standard values for high-pressure gas jets. Higher values of p are difficult to achieve in reality because of the transverse divergence of the gas flow exiting the nozzle. By tilting the gas jet in the plane of laser incidence the density profile along the laser axis will have the form $n \sim \exp[-(x-x_0)^p/(\sigma\ \cos\theta)^p]/[1-\tan\theta\ \tan\alpha(x-x_0)/\sigma]^2$, where α is the half opening angle of the gas flow and θ is the tilting angle. This expression is presented by the blue line in Fig. 2(a), where the gas divergence is $\alpha = 30^\circ$ and $\theta = 40^\circ$. However, in the simulation we used a simple super-Gaussian profile with $p = 6$ and $\sigma = 50$ μm, which has almost the same density slope as the tilted gas jet. The center of the gas jet is at 50 μm distance from the left boundary, which is at $x = -30$ μm, where the laser pulse is launched from. The oxygen density in the plateau region is twice of the hydrogen density $n_H = 7.4 \times 10^{18}$ cm^{-3}.

In order to assess the neutron flux, we perform Geant4v.11.0.2 based Monte Carlo simulation [39]. Using particle data from the PIC simulations, as the parameters of the primary particle (deuteron), the collision with a 100-μm-thick tritiated water target was considered. In this simulation the QGSP-BIC-AllHP predefined physics list and the TENDL nuclear data library were used. During the simulation, the position, direction of propagation, and the kinetic energy of generated neutron was recorded.

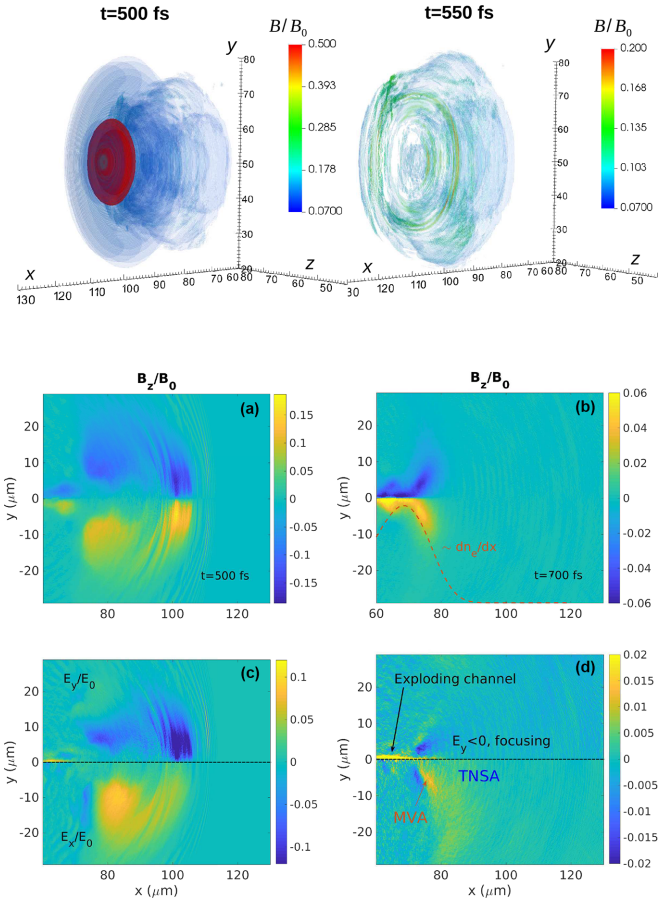

FIG. 3. (Top) Distribution of the transverse magnetic field at two time instances in 3D. The laser pulse (visible at $t = 500$ fs) propagates in the positive x direction. Azimuthal magnetic field (a), (b) and electric fields (c), (d) are shown at two time instances. In (c) and (d) below the axis of symmetry ($y = 0$) the longitudinal field is shown, while above the transversal (or radial) electric field. In (b) the red dashed line represents the derivative of the density profile (in arbitrary units), which indicates that the magnetic vortex is generated at the position of the maximum density gradient.

III. RESULTS

In an earlier work we investigated the acceleration of protons from a narrow (≈50-μm-wide) high-density ($n_H \approx 0.1 n_c$) gas-jet target driven by few cycle TW-class laser pulses in 2D geometry [36]. The main finding was that in the initial stage of the acceleration a strong magnetic vortex [40] is generated at the rear side of a round gas jet which enhances the longitudinal electric field generated by the strong transient current. This electric field launches an ionic wave which propagates down in the decaying density profile and breaks after few picoseconds of propagation. This process is accompanied with acceleration by a sheath electric field since the electrons are hot and trigger a charge separation field in the density down ramp, which has a larger extension compared to the vortex size. These two types of electric fields appear close to each other in space. For instance, if the density profile is described by the function $n = n_0 \exp[-(x-x_0)^p/\sigma^p]$, where x_0 is the center of the gas jet along the laser propagation axis and σ defines the width of the target, then the position of the magnetic vortex is $x_m = \sigma(1-1/p)^{1/p}$ and the center of the target-normal sheath acceleration (TNSA) like field is at [36] $x_s \approx 1.1\sigma + 0.08\sigma^2/(\lambda_D p^2)$, where λ_D is the Debye length.

In the case of sharper density profiles these fields almost or completely overlap, but they are separated when p is small. By solving numerically the equation $x_s - x_m \leqslant \lambda_D$ (assuming $\sigma/\lambda_D \approx 100$) we found that the value $p = 6$ is a good choice, which ensures the soliton propagation without early wave breaking and provides a strong charge-separation field near the edge of the gas jet, as it is explained in Sec. IV.

For a more quantitative analysis of the interaction we performed the simulations in 3D with initial parameters very similar to those used in Ref. [36]. The isocontours of the laser magnetic fields ($B = \sqrt{B_y^2 + B_z^2}$) and the surrounding plasma fields are shown in Fig. 3 at $t = 500$ fs, normalized to the relativistic threshold value $B_0 = m_e\omega_0/e$. A little later (at 550 fs) the laser pulse leaves completely the plasma leaving behind a ring-shaped magnetic field which expands radially. This consists of two waves: one is the surface plasma wave,

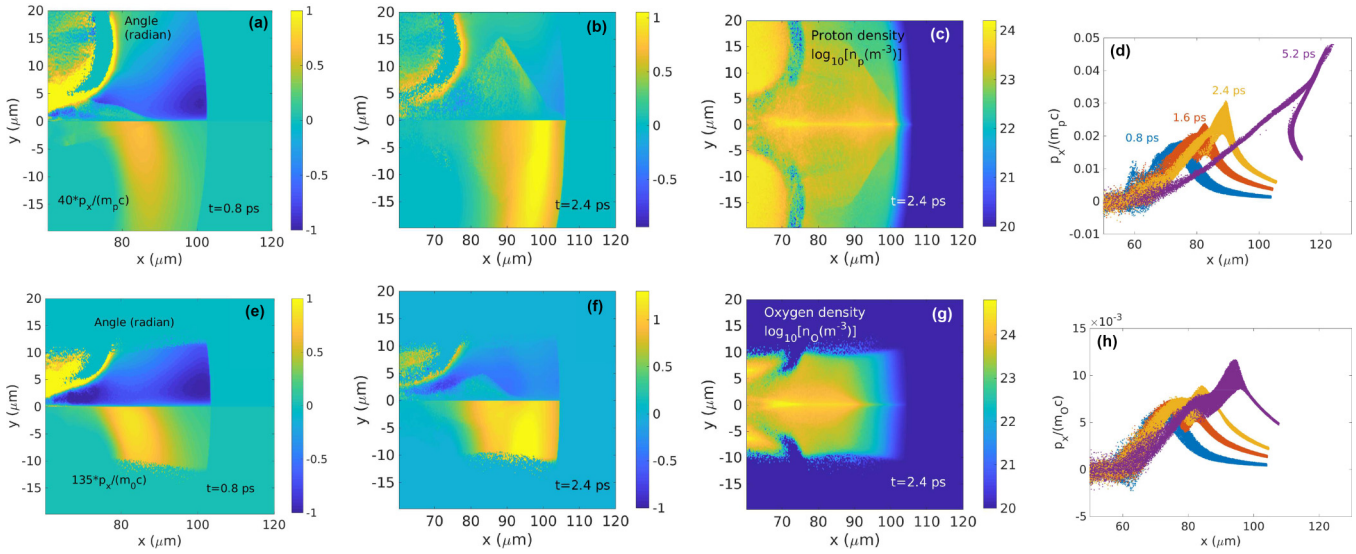

FIG. 4. Momentum and angle distribution of protons (a), (b) and O^{6+} (e), (f). In all pictures particles with propagation angle less then 60° are included. The upper half plane shows the actual angle of propagation in the xy plane, while the lower half plane presents the distribution of longitudinal momentum of ions, which is multiplied by a numeric factor to be presented by the same color scale. In (c) and (g) the spatial density distributions are shown at $t = 2.4$ ps, on logarithmic scale. In (d) and (h) the proton and oxygen ion phase-space distributions are shown at different time instances.

which propagates transversely in the low-density plasma, and the second is associated with the coherent transition radiation.

A more detailed picture of the generated field is shown in Fig. 3(a), which is the cross section of the 3D domain at $z = 0$. The strong magnetic field corresponds to the short-wavelength radiation generated behind the laser pulse, which is near the position $x = 110$ μm at this time instance. Behind this region we find the two magnetic vortices: one is expanding radially (near $x = 80$ μm), while the second stays close to the axis, that is inside the channel. The acceleration basically consists of two stages: first transient high fields appear due to electron cavitation and laser-driven currents [Figs. 3(a) and 3(c)], then the plasma evolves self-consistently, where the electron current feeds the azimuthal magnetic field around the central channel [Figs. 3(b) and 3(d), for more details and plasma evolution see Appendix A (Fig 8) and Appendix B (Fig. 12)]]. In earlier works [40,41] it has been shown that the azimuthal magnetic field at the plasma-vacuum interface can trigger strong charge separation via the gradients of the magnetic energy density (magnetic pressure), which is visible also in Fig. 3. It is important to note that the transversal field associated to the vortex is a focusing field for ions. In Fig. 3(b) (200 fs later) the magnetic field is still strong and at the position of the B-field gradients strong electric fields appear [see Fig. 3(d)]. The red dashed line indicates that the magnetic vortex is generated at the position of the highest density gradient. Aside from these induced fields there are Coulomb (or charge-separation) fields as well: longitudinal charge-separation field inside the density ramp (TNSA field) and radial Coulomb field, causing explosion of the plasma channel.

The action of the electromagnetic fields on the ions is presented in Fig. 4. The upper row shows the evolution of the proton distribution, while the lower row is for O^{6+}. There are very few oxygen ions with higher charge state in this portion of the plasma. At early times [Figs. 4(a) and 4(e)] the ion distribution resembles the fields shown in Fig. 3, which means that they get focused in the decaying plasma profile and get accelerated in the forward direction near the position of the magnetic vortex (between $x = 70$ and 80 μm). The radial explosion of protons is much faster since they are lighter, which is visible in the angular distribution in Fig. 4(a). The radial motion of oxygen becomes visible after 2 ps [see Figs. 4(b) and 4(f)], which is accompanied with a significant longitudinal drift. It is important to note that the highly divergent ions have lower energy and they are not at the location of high p_x. This feature allows the generation of highly collimated, ultrashort, and low-divergence proton beams. From the longitudinal phase space one can see that the ion peak velocity increases, which is explained by the soliton propagation in a density down ramp [36]. It is also noticeable that the light and heavy ions almost copropagate for a relatively long time (≈2 ps), which results in the additional acceleration of protons in the field of the heavy-ion soliton, like in the Coulomb-piston effect [42]. In principle the heavy ions gain A/Z times lower momentum in an accelerating field, compared to the protons, where A is the atomic number and Z is the charge state. Therefore, the oxygen velocity is about 2.7 times lower and the fastest protons get separated from the heavy ions, which is seen in Figs. 4(d) and 4(h).

Although the energy boost of protons does not last long, the spectral shape can be significantly altered, when heavier ions are also present in the gas. In order to show the difference the exact same simulation was performed with only hydrogen, that is, $n_H = n_e = 10^{20}$ cm^{-3}. The final proton spectra in the two cases are shown in Fig. 5, where the white lines show the spectra within a cone angle of $\theta < 4°$ (in the case of gas mixture) and $\theta < 6°$ (in the case of pure hydrogen gas). The emission angle is defined as $\theta = \arctan(p_r/p_x)$, where $p_r = \sqrt{p_y^2 + p_z^2}$. If oxygen is also included in the gas, then the

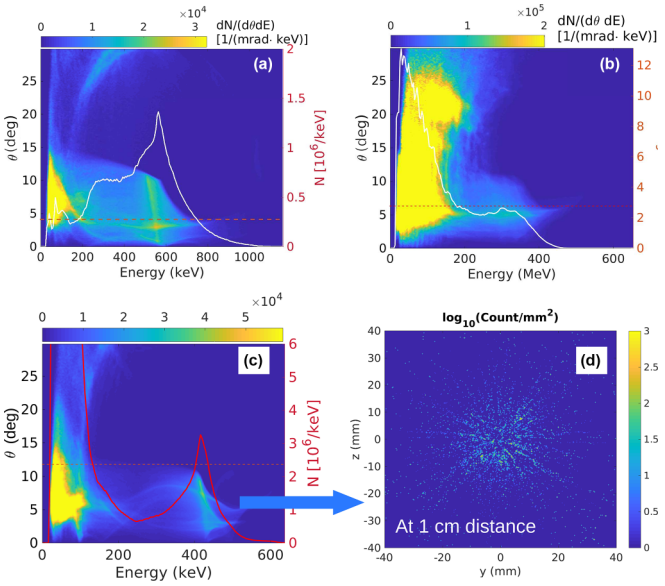

FIG. 5. Proton angular-energy distribution (from $x > 90$ μm) at 6 ps with (a) and without oxygen (b) present in the gas. The white lines show the integrated spectra in the angular interval below the red dashed lines. In (c) the deuteron spectrum is for the case presented in (a), but instead of hydrogen, deuterium was used. After the interaction with a tritium-rich target placed at 1 cm distance the resulting neutron distribution in the transversal plane is shown in (d) at the time instance when the slowest ion reaches the target surface. In the neutron production only energetic ions are included with energy larger than 200 keV.

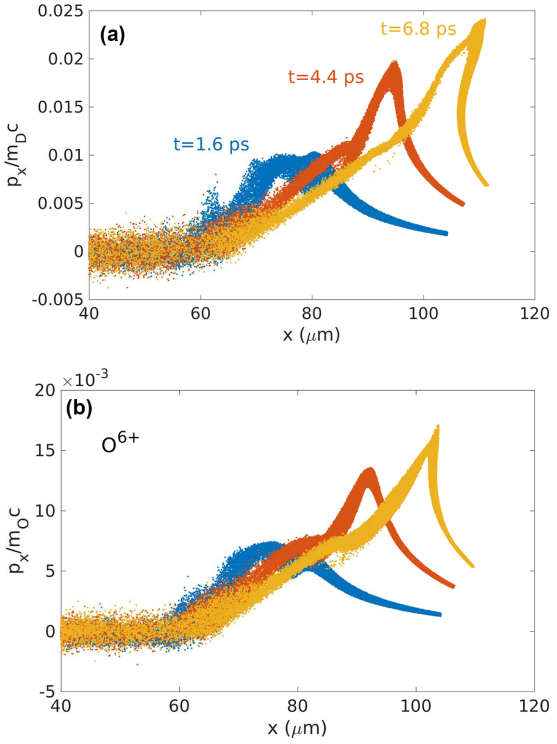

FIG. 6. Phase-space distribution of deuteron (upper) and oxygen (lower) ions at different time instances.

proton energy is much higher and the spectrum is peaked near the middle of the spectral range (close to 600 keV), although the proton number is smaller than in the of single-ion species [Fig. 5(b)]. It is important to note that the propagation direction of the proton bunch is nonaxial, there is a ≈5° deviation, which is caused by the asymmetric field generation in the xz plane (see Appendix B). This is associated with the short duration of the laser pulse, leading to the few-cycle effects described in Refs. [43,44]. During the pulse propagation in the dense plasma the carrier envelope phase and the laser envelope change significantly and the intensity distribution is no longer centered when the pulse reaches the rear side of the plasma. One can correct this asymmetry by using longer pulses [45].

The separation of light and heavy ions in phase space is well understood in theoretical models [46], where heavy-ion dominance is assumed. The separation can be delayed if the charge-to-mass ratio of the two species is similar, which we can achieve by considering deuterium instead of hydrogen. Such a case is presented in Fig. 6 which clearly shows that the D^+ and O^{6+} ions move together, the ion separation happens after 4 ps. The resulting energy spectrum is shown in Fig. 5(c), where a more pronounced spectral peak is found, but the angular divergence of light ions is much larger than in the case of pure hydrogen. The reason is that the heavy ions push the deuterons not only in the forward direction, but also radially while they copropagate, thus the divergence increases. Similar spectral peaks have been observed in experiments as well, where water droplets were used as mass-limited targets [47].

In Fig. 5(d) the spatial distribution of neutrons is shown (projected into the transverse plane) right after the interaction of the D^+ ions with a foil target, which contains tritium, placed at 1 cm distance from the gas jet. The total number of generated neutrons is 1.5×10^5 and the total yield is almost the same when deuterium was used instead of tritium. The neutrons fly in all directions and the radial width of this spherical shell is about 5 mm, resulting in 0.20-ns duration at $\approx 2.5 \times 10^7$ m/s average velocity. The density (or duration) of this neutron burst can be reduced even more by placing the second target closer to the ion source.

IV. DISCUSSION

For efficient light-ion acceleration the solitary wave should not break, which is ensured by maintaining the condition [36] $v_s - v_0 > \sqrt{e\phi_s/m_i}$, where v_s and v_0 are the soliton and background plasma velocities, respectively, ϕ_s is the potential difference across the soliton, and m_i is the ion mass. The initial velocity of the soliton is defined by the pulse duration [it defines the lifetime of magnetic vortex acceleration (MVA)], while the velocity of the expanding plasma is mostly defined by the density scale length (σ in our case). A simplified schematics in Fig. 7 illustrates the relation between plasma fields and ion phase-space curves in the case of short and long plasma gradients. In the case of a sharper density profile the MVA and TNSA fields overlap and the latter dominates. The modulation in the ion distribution is a marginal effect in this case. If the density is smoother (larger σ) these two fields are

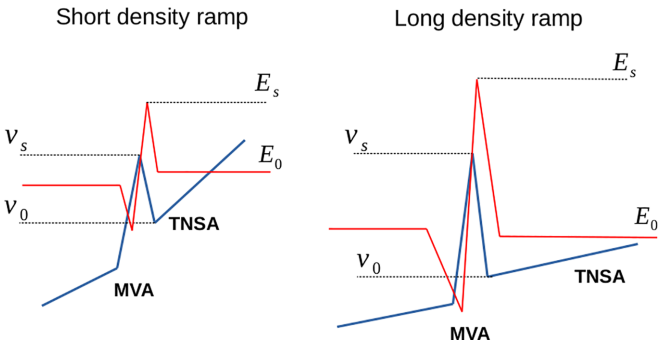

FIG. 7. Red lines represent the longitudinal electric field profiles, while the blue lines depict the ion phase-space distribution for short and long density ramps.

well separated and the MVA can be effective providing a large jump in the ion velocity along the propagation axis. This ion wave propagates downward in the density ramp and its stability is decided by the wave-breaking condition, written above. The electric field acting in the TNSA region (also called as self-similar field) can be expressed as [48,49] $E_0 = T_h/l_n$, where $l_n \propto \sigma$ is the density scale length. An optimum value of σ exists because if it is too large, then the difference between E_s and E_0 can be large enough for early wave breaking.

The final energy of light ions is defined by the separation time of the two (heavy and light) solitons presented in Figs. 4(d) and 4(h). The initial velocity of these solitons is given by $v_{(l,h)0} = eZ_{l,h}E_x t_a/(A_{l,h}m_p)$, where the subscripts denote light and heavy ions, E_x is the average electric field acting on both ions for a time t_a. Typically, t_a is on the order of several hundreds of femtoseconds for ultrashort pulses. For efficient Coulomb-piston effect the ion solitons should not be neutralized by the electrons, which requires $L_s <\approx \lambda_D$, which is valid in the decaying density ramp used in our simulation, where L_s is the width of the soliton and $\lambda_D = \sqrt{\epsilon_0 T_h/(e^2 n_e)}$ is the Debye length with average electron temperature $T_h \sim 0.5$ MeV. The time required for complete separation (t_s) can be calculated from the equations

$$\int_0^{t_s} (v_l - v_h)dt = L_s/2, \tag{1}$$

$$v_l(t) = f v_{l0} + eZ_l E_s t/(A_l m_p), \tag{2}$$

where E_s is the electrostatic field generated by the space charge of heavy ions and $1.5 < f < 2$ is a factor defining the velocity increase of the heavy soliton during its propagation in the decaying density profile [50]. It is important to note that these equations are valid before the wave breaking of the heavy-ion soliton, thus, one important condition is $t_{\rm wb} \gg t_s$, where $t_{\rm wb}$ is the wave-breaking time [36]. The final velocity of the light ions, which contribute to the spectral peak, is then calculated as $v_{l,p} = v_l(t_s)$. The energy cutoff, which is higher, is acquired due to wave breaking of the light-ion soliton, if it occurs. The solution of Eqs. (1) and (2) is

$$t_s = \frac{A_l m_p}{eZ_l E_s}\left[f v_{h0} - f v_{l0} + \sqrt{(f v_{h0} - f v_{l0})^2 + \frac{2W_l}{A_l m_p}}\right], \tag{3}$$

where $W_l = eZ_l E_s L_s/2$ is the energy gained in the electrostatic potential of the heavy-ion soliton. By substituting Eq. (3) into (2) we arrive to the velocity of light-ion soliton after separation:

$$\frac{v_{l,p}}{v_{l0}} = fM + \sqrt{[f(M-1)]^2 + W_l/W_0}, \tag{4}$$

where $M = v_{h0}/v_{l0} = (Z_h/A_h)(Z_l/A_l)^{-1} \leqslant 1$ and $W_0 = A_l m_p v_{l0}^2/2$. One can see that the final energy is higher if M is larger and the electric field of the soliton has to be large, compared to the induced electric field (E_x), which means that the heavy ions should dominate inside the plasma. For typical parameters, $f \approx 2$ and $M \approx 0.5$, the velocity enhancement can be expressed expressed as $v_{l,p}/v_{l0} = 1 + \sqrt{1 + W_l/W_0}$. It is easily shown that for protons $W_l/W_0 \approx 2E_s^2/(E_x^2\tau_a^2)$, where $\tau_a = \omega_p t_a$ with $\omega_p = (n_e e^2/m_p\epsilon_0)^{1/2}$. This ratio is typically less than one, but even for $W_l/W_0 \ll 1$ the energy enhancement in the density down ramp is at least a factor of 4.

V. CONCLUSIONS

We presented a very complex acceleration scheme, which is possible to realize experimentally using ultrashort pulses of intensities above 10^{19} W/cm^2 interacting with a gas jet containing a mixture of heavy and light ions. We anticipate the existence of an optimal density scale length for producing monoenergetic ion bunches, which can be easily verified experimentally by changing the tilting angle of a supersonic gas jet, as it is presented in Fig. 1. The low pulse energy and the gas phase of the target allow the light-ion acceleration up to MeV energy at high repetition rate (100–1000 Hz). The generated proton (or deuteron) bunch has relatively high-energy density: 10^8 particles with 0.5 MeV average energy ($\sim$10 μJ) in $\sim$10 μm^3 volume. The angle of propagation of ions is close to 5° (not axial), due to the few-cycle length of the pulses, but at high repetition rate the average particle density on the irradiated surface would be centered and smoothed. Our three-dimensional simulations give quantitative results from the interaction of few-cycle pulses with near-critical density plasma, which is an important step towards experimental realization of a source providing very compact, spatially compressed, low-energy-spread ion bunches. As a possible application, we presented the applicability of the generated deuterium bunch as a pointlike fast neutron source, producing more then 10^5 neutrons in one shot.

ACKNOWLEDGMENTS

We acknowledge support of the Department of Information Services and Computing, Helmholtz-Zentrum Dresden-Rossendorf (HZDR), Germany, for providing access to the Compute Cluster Hemera. We acknowledge KIFÜ/NIIF for awarding us access to HPC resource based in Debrecen, Hungary. The ELI-ALPS project (Project No. GINOP-2.3.6-15-2015-00001) is supported by the European Union and cofinanced by the European Regional Development Fund. The authors also acknowledge the Project No. 2020-1.2.4-TÉT-IPARI-2021-00018, named as HUN-CHI TéT, which is supported by the National Research, Development and Innovation Fund of Hungary.

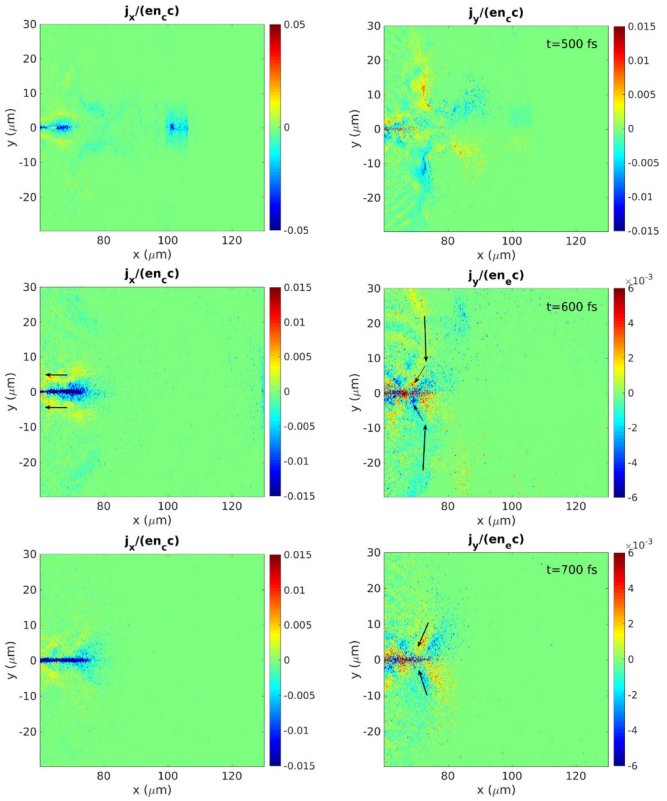

FIG. 8. Longitudinal (left column) and transverse (right column) current density components in the xy plane at different time instances.

APPENDIX A: EVOLUTION OF CURRENT DENSITY AT THE EXIT SIDE OF THE GAS JET

The spatial distributions of current densities are shown in Fig. 8 for the case presented in Fig. 2 in the main text. One can see the strong axial current at $t = 500$ fs, which contains the electrons following the laser pulse. At this time instance there is a very strong radial current density which intends to neutralize the positive charge in the ion channel along the laser propagation axis. This strong current generates a radial electric field locally and accelerates the ions outward from the center, which results in a large radial velocity component and large angle of propagation. The position of this instantaneous return current is clearly visible in Fig. 3 of the main text, where the ion propagation angle is larger than 60°.

Later on the electrons continue to flow outside from the channel, which is compensated by a return current near the wall of the channel. We observe significant radial current as well (at 600 and 700 fs) near the end of the channel, which is responsible for the B-field generation, which is presented in the main text (Fig. 2) and in Fig 11 of this paper.

APPENDIX B: ASYMMETRIC ACCELERATION IN CASE OF LINEAR POLARIZATION

In Fig. 9 we present the field distributions in the xz plane, which is the plane of polarization of the laser pulse. One can see significant asymmetry, with respect to the axis of propagation, in the azimuthal magnetic field as well as in the longitudinal electric field.

The difference in accelerating fields above and below the axis ($z = 0$) results in difference in the momentum distribution, which is shown in Fig. 10. Although the asymmetry in acceleration is small it results in ∼5° deviation, which is shown in the main text.

The asymmetry is present only in the plane of polarization of the laser field, in the orthogonal plane everything looks symmetric, as it is shown in Fig. 11. Here we show that after the transient EM fields propagate far from the axis, there is still an electric current inside the channel and a return current inside the plasma skin depth that generates an azimuthal magnetic field. This magnetic field decays slowly and the electric fields appear due to the charge separation driven by the magnetic pressure gradients. The modulation in the electron density caused by the B field is shown in Fig. 12, which shows the formation of a bubble (or ion cavity) at the moment when the laser pulse crosses the density down ramp ($t = 400$ fs). The high-density electron bunch along the propagation axis attracts the ions, thus, they move radially towards the axis and form a high-density column, which later acts on electrons, as it is seen in Fig. 12. Note that the electron plasma period is only 11 fs. Later, due to the magnetic pressure inside the channel, a conelike shape (or funnel) appears, which resembles the shape of the B field shown in Fig. 11. At the end of the central column (around $x = 80$ μm) the protons experience the Coulomb field of the concentrated oxygen ions and the focusing field generated by the magnetic vortex (see the red ellipse in Fig 11), while they are accelerated forward at the same time. In this limited spatial domain this unique field configuration results in the generation of highly collimated short proton bunches.

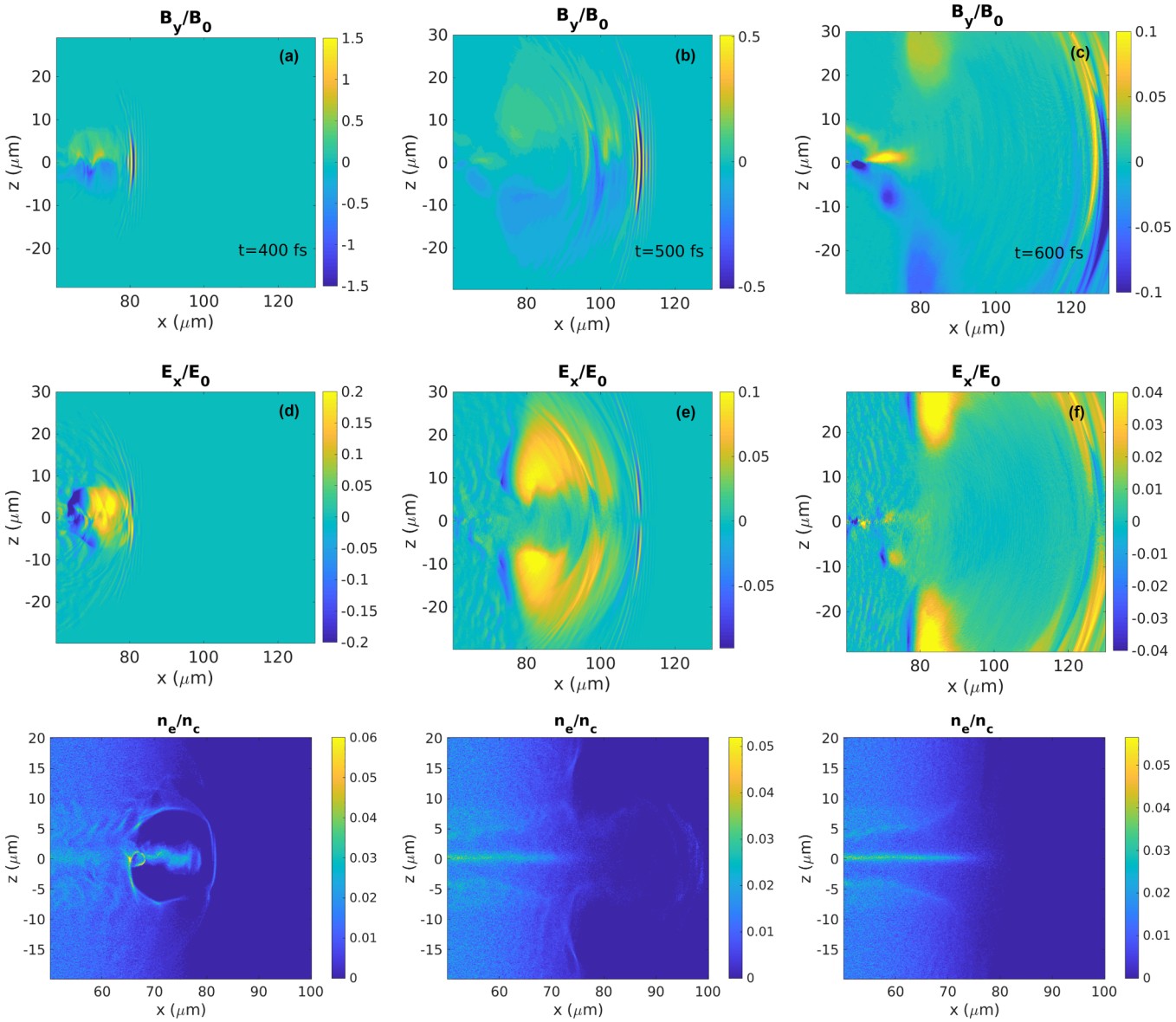

FIG. 9. Azimuthal magnetic field (a)–(c) and forward accelerating electric field (d)–(f) in the *xz* plane. The pictures are produced from the simulations presented in Figs. 2 and 3. Below the electron density distributions are shown at the same time instances.

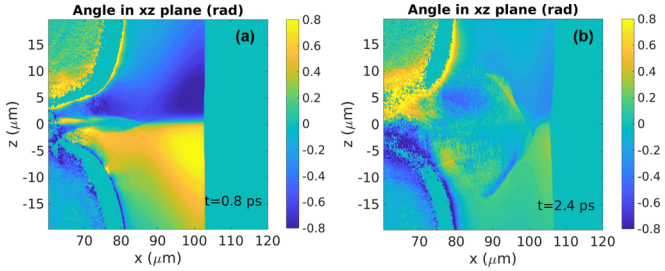

FIG. 10. Propagation angle of protons in the *xz* cross section of the simulation domain.

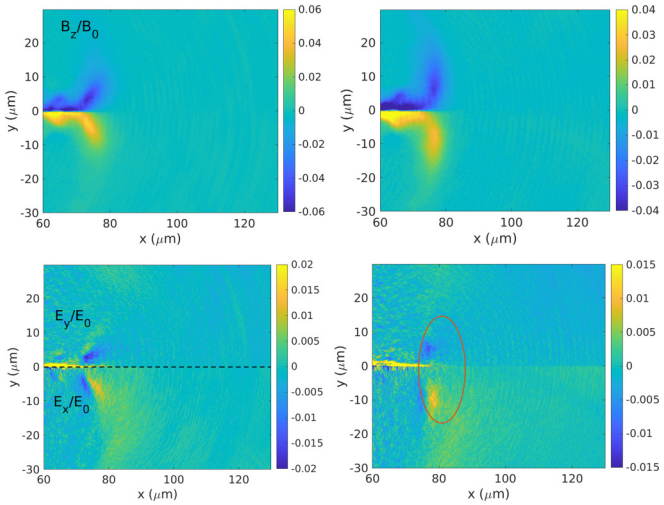

FIG. 11. Azimuthal magnetic field (upper row) and electric fields (lower row) in the *xy* plane. These pictures present the continuation of Fig. 9. The time instance is 700 fs (left) and 800 fs (right). The red ellipse illustrates the position where the high-energy protons originate from. Focusing and accelerating fields are both present in this region.

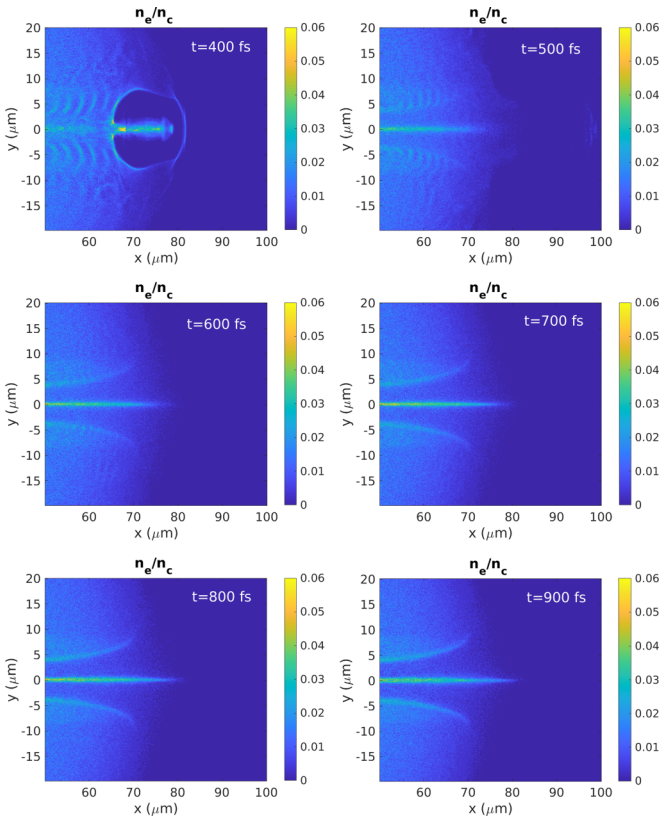

FIG. 12. Evolution of the electron density in the *xy* plane.

[1] H. Daido, M. Nishiuchi, and A. S. Pirozhkov, Review of laser-driven ion sources and their applications, Rep. Prog. Phys. **75**, 056401 (2012).

[2] M. Borghesi, P. Audebert, S. V. Bulanov, T. Cowan, J. Fuchs, J. C. Gauthier, A. J. Mackinnon, P. K. Patel, G. Pretzler, L. Romagnani *et al.*, High-intensity laser-plasma interaction

studies employing laser-driven proton probes, Laser Part. Beams **23**, 291 (2005).

[3] A. J. Mackinnon, P. K. Patel, R. P. Town, M. J. Edwards, T. Phillips, S. C. Lerner, D. W. Price, D. Hicks, M. H. Key, S. Hatchett, S. C. Wilks, M. Borghesi, L. Romagnani, S. Kar, T. Toncian, G. Pretzler, O. Willi, M. Koenig, E. Martinolli, S. Lepape *et al.*, Proton radiography as an electromagnetic field and density perturbation diagnostic (invited), Rev. Sci. Instrum. **75**, 3531 (2004).

[4] L. Romagnani, J. Fuchs, M. Borghesi, P. Antici, P. Audebert, F. Ceccherini, T. Cowan, T. Grismayer, S. Kar, A. Macchi, P. Mora, G. Pretzler, A. Schiavi, T. Toncian, and O. Willi, Dynamics of Electric Fields Driving the Laser Acceleration of Multi-MeV Protons, Phys. Rev. Lett. **95**, 195001 (2005).

[5] T. Sokollik, M. Schnürer, S. Ter-Avetisyan, P. V. Nickles, E. Risse, M. Kalashnikov, W. Sandner, G. Priebe, M. Amin, T. Toncian, O. Willi, and A. A. Andreev, Transient electric fields in laser plasmas observed by proton streak deflectometry, Appl. Phys. Lett. **92**, 091503 (2008).

[6] F. Abicht, J. Braenzel, G. Priebe, Ch. Koschitzki, A. A. Andreev, P. V. Nickles, W. Sander, and M. Schnürer, Tracing dynamics of laser-induced fields on ultrathin foils using complementary imaging with streak deflectometry, Phys. Rev. Accel. Beams **19**, 091302 (2016).

[7] A. Macchi, M. Borghesi, and M. Passoni, Ion acceleration by superintense laser-plasma interaction, Rev. Mod. Phys. **85**, 751 (2013).

[8] V. Dangendorf and R. Zboray, Potential and status in imaging with fast neutrons, Neutron News **26**, 27 (2015).

[9] M. Zimmer, S. Scheuren, A. Kleinschmidt, N. Mitura, A. Tebartz, G. Schaumann, T. Abel, T. Ebert, M. Hesse, Ş. Zähter, S. C. Vogel, O. Merle, R.-J. Ahlers, S. Duarte Pinto, M. Peschke, T. Kröll, V. Bagnoud, C. Rödel, and M. Roth, Demonstration of non-destructive and isotope-sensitive material analysis using a short-pulsed laser-driven epi-thermal neutron source, Nat. Commun. **13**, 1173 (2022).

[10] T. Ditmire, J. Zweiback, V. P. Yanovsky, T. E. Cowan, G. Hays, and K. B. Wharton, Nuclear fusion from explosions of femtosecond laser-heated deuterium clusters, Nature (London) **398**, 489 (1999).

[11] M. Roth, D. Jung, K. Falk, N. Guler, O. Deppert, M. Devlin, A. Favalli, J. Fernandez, D. Gautier, M. Geissel, R. Haight, C. E. Hamilton, B. M. Hegelich, R. P. Johnson, F. Merrill, G. Schaumann, K. Schoenberg, M. Schollmeier, T. Shimada, T. Taddeucci *et al.*, Bright Laser-Driven Neutron Source Based on the Relativistic Transparency of Solids, Phys. Rev. Lett. **110**, 044802 (2013).

[12] A. Kleinschmidt, V. Bagnoud, O. Deppert, A. Favalli, S. Frydrych, J. Hornung, D. Jahn, G. Schaumann, A. Tebartz, F. Wagner, G. Wurden, B. Zielbauer, and M. Roth, Intense, directed neutron beams from a laser-driven neutron source at phelix, Phys. Plasmas **25**, 053101 (2018).

[13] A. Alejo, A. G. Krygier, H. Ahmed, J. T. Morrison, R. J. Clarke, J. Fuchs, A. Green, J. S. Green, D. Jung, A. Kleinschmidt, Z. Najmudin, H. Nakamura, P. Norreys, M. Notley, M. Oliver, M. Roth, L. Vassura, M. Zepf, M. Borghesi, R. R. Freeman *et al.*, High flux, beamed neutron sources employing deuteron-rich ion beams from D_2O-ice layered targets, Plasma Phys. Controlled Fusion **59**, 064004 (2017).

[14] S. R. Mirfayzi, A. Yogo, Z. Lan, T. Ishimoto, A. Iwamoto, M. Nagata, M. Nakai, Y. Arikawa, Y. Abe, D. Golovin, Y. Honoki, T. Mori, K. Okamoto, S. Shokita, D. Neely, S. Fujioka, K. Mima, H. Nishimura, S. Kar, and R. Kodama, Proof-of-principle experiment for laser-driven cold neutron source, Sci. Rep. **10**, 20157 (2020).

[15] M. Chadha M. D., J. Capala, J. A. Coderre, E. H. Elowitz, J. Iwai, D. D. Joel, H. B. Liu, L. Wielopolski, and A. D. Chanana, Boron neutron-capture therapy (BNCT) for glioblastoma multiforme (GBM) using the epithermal neutron beam at the brookhaven national laboratory, Int. J. Radiat. Oncol. Biol. Phys. **40**, 829 (1998).

[16] F. Wagner, O. Deppert, C. Brabetz, P. Fiala, A. Kleinschmidt, P. Poth, V. A. Schanz, A. Tebartz, B. Zielbauer, M. Roth, T. Stöhlker, and V. Bagnoud, Maximum Proton Energy Above 85 Mev from the Relativistic Interaction of Laser Pulses with Micrometer Thick CH_2 Targets, Phys. Rev. Lett. **116**, 205002 (2016).

[17] N. P. Dover, T. Ziegler, S. Assenbaum, C. Bernert, S. Bock, F.-E. Brack, T. E. Cowan, E. J. Ditter, M. Garten, L. Gaus, I. Goethel, G. S. Hicks, H. Kiriyama, T. Kluge, J. K. Koga, A. Kon, K. Kondo, S. Kraft, F. Kroll, H. F. Lowe *et al.*, Enhanced ion acceleration from transparency-driven foils demonstrated at two ultraintense laser facilities, Light Sci. Appl. **12**, 71 (2023).

[18] P. K. Patel, A. J. Mackinnon, M. H. Key, T. E. Cowan, M. E. Foord, M. Allen, D. F. Price, H. Ruhl, P. T. Springer, and R. Stephens, Isochoric Heating of Solid-Density Matter with an Ultrafast Proton Beam, Phys. Rev. Lett. **91**, 125004 (2003).

[19] A. Yogo, K. Sato, M. Nishikino, M. Mori, T. Teshima, H. Numasaki, M. Murakami, Y. Demizu, S. Akagi, S. Nagayama, K. Ogura, A. Sagisaka, S. Orimo, M. Nishiuchi, A. S. Pirozhkov, M. Ikegami, M. Tampo, H. Sakaki, M. Suzuki, I. Daito *et al.*, Application of laser-accelerated protons to the demonstration of dna double-strand breaks in human cancer cells, Appl. Phys. Lett. **94**, 181502 (2009).

[20] K. W. D. Ledingham, J. Magill, P. McKenna, J. Yang, J. Galy, R. Schenkel, J. Rebizant, T. McCanny, S. Shimizu, L. Robson, R. P. Singhal, M. S. Wei, S. P. D. Mangles, P. Nilson, K. Krushelnick, R. J. Clarke, and P. A. Norreys, Laser-driven photo-transmutation of ^{129}I-A long-lived nuclear waste product, J. Phys. D: Appl. Phys. **36**, L79 (2003).

[21] P. K. Singh, P. Varmazyar, B. Nagy, J.-G. Son, S. Ter-Avetisyan, and K. Osvay, Low divergent mev-class proton beam with micrometer source size driven by a few-cycle laser pulse, Sci. Rep. **12**, 8100 (2022).

[22] J. I. Apiñaniz, S. Malko, R. Fedosejevs, W. Cayzac, X. Vaisseau, D. de Luis, G. Gatti, C. McGuffey, M. Bailly-Grandvaux, K. Bhutwala, V. Ospina-Bohorquez, J. Balboa, J. J. Santos, D. Batani, F. Beg, L. Roso, J. A. Perez-Hernandez, and L. Volpe, A quasi-monoenergetic short time duration compact proton source for probing high energy density states of matter, Sci. Rep. **11**, 6881 (2021).

[23] J. T. Morrison, S. Feister, K. D. Frische, D. R. Austin, G. K. Ngirmang, N. R. Murphy, C. Orban, E. A. Chowdhury, and W. M. Roquemore, Corrigendum: MeV proton acceleration at kHz repetition rate from ultra-intense laser liquid interaction, New J. Phys. **20**, 069501 (2018).

[24] A. Thoss, M. Richardson, G. Korn, M. Faubel, H. Stiel, U. Vogt, and T. Elsaesser, Kilohertz sources of hard x rays and fast ions

with femtosecond laser plasmas, J. Opt. Soc. Am. B **20**, 224 (2003).

[25] A. Lifschitz, F. Sylla, S. Kahaly, A. Flacco, M. Veltcheva, G. Sanchez-Arriaga, E. Lefebvre, and V. Malka, Ion acceleration in underdense plasmas by ultra-short laser pulses, New J. Phys. **16**, 033031 (2014).

[26] P. K. Singh, V. B. Pathak, J. H. Shin, I. W. Choi, K. Nakajima, S. K. Lee, J. H. Sung, H. W. Lee, Y. J. Rhee, C. Aniculaesei, C. M. Kim, K. H. Pae, M. H. Cho, C. Hojbota, S. G. Lee, F. Mollica, V. Malka, C.-M. Ryu, H. T. Kim, and C. H. Nam, Electrostatic shock acceleration of ions in near-critical-density plasma driven by a femtosecond petawatt laser, Sci. Rep. **10**, 18452 (2020).

[27] M. S. Wei, S. P. D. Mangles, Z. Najmudin, B. Walton, A. Gopal, M. Tatarakis, A. E. Dangor, E. L. Clark, R. G. Evans, S. Fritzler, R. J. Clarke, C. Hernandez-Gomez, D. Neely, W. Mori, M. Tzoufras, and K. Krushelnick, Ion Acceleration by Collisionless Shocks in High-Intensity-Laser–Underdense-Plasma Interaction, Phys. Rev. Lett. **93**, 155003 (2004).

[28] M. H. Helle, D. F. Gordon, D. Kaganovich, Y. Chen, J. P. Palastro, and A. Ting, Laser-Accelerated Ions from a Shock-Compressed Gas Foil, Phys. Rev. Lett. **117**, 165001 (2016).

[29] S. N. Chen, M. Vranic, T. Gangolf, E. Boella, P. Antici, M. Bailly-Grandvaux, P. Loiseau, H. Pépin, G. Revet, J. J. Santos, A. M. Schroer, M. Starodubtsev, O. Willi, L. O. Silva, E. d'Humières, and J. Fuchs, Collimated protons accelerated from an overdense gas jet irradiated by a 1 μm wavelength high-intensity short-pulse laser, Sci. Rep. **7**, 13505 (2017).

[30] L. Willingale, S. P. D. Mangles, P. M. Nilson, R. J. Clarke, A. E. Dangor, M. C. Kaluza, S. Karsch, K. L. Lancaster, W. B. Mori, Z. Najmudin, J. Schreiber, A. G. R. Thomas, M. S. Wei, and K. Krushelnick, Collimated Multi-MeV Ion Beams from High-Intensity Laser Interactions with Underdense Plasma, Phys. Rev. Lett. **96**, 245002 (2006).

[31] S. Tochitsky, A. Pak, F. Fiuza, D. Haberberger, N. Lemos, A. Link, D. H. Froula, and C. Joshi, Laser-driven collisionless shock acceleration of ions from near-critical plasmas, Phys. Plasmas **27**, 083102 (2020).

[32] C. A. J. Palmer, N. P. Dover, I. Pogorelsky, M. Babzien, G. I. Dudnikova, M. Ispiriyan, M. N. Polyanskiy, J. Schreiber, P. Shkolnikov, V. Yakimenko, and Z. Najmudin, Monoenergetic Proton Beams Accelerated by a Radiation Pressure Driven Shock, Phys. Rev. Lett. **106**, 014801 (2011).

[33] D. Haberberger, S. Tochitsky, F. Fiuza, C. Gong, R. A. Fonseca, L. O. Silva, W. B. Mori, and C. Joshi, Collisionless shocks in laser-produced plasma generate monoenergetic high-energy proton beams, Nat. Phys. **8**, 95 (2012).

[34] L. Rovige, J. Huijts, A. Vernier, I. Andriyash, F. Sylla, V. Tomkus, V. Girdauskas, G. Raciukaitis, J. Dudutis, V. Stankevic, P. Gecys, and J. Faure, Symmetric and asymmetric shocked gas jets for laser-plasma experiments, Rev. Sci. Instrum. **92**, 083302 (2021).

[35] F. Sylla, M. Veltcheva, S. Kahaly, A. Flacco, and V. Malka, Development and characterization of very dense submillimetric gas jets for laser-plasma interaction, Rev. Sci. Instrum. **83**, 033507 (2012).

[36] Z. Lécz, A. Sharma, A. Andreev, J. Fülöp, and C. Kamperidis, Sliding-wave acceleration of ions in high-density gas jet targets, Phys. Rev. E **103**, 053210 (2021).

[37] K. Schmid and L. Veisz, Supersonic gas jets for laser-plasma experiments, Rev. Sci. Instrum. **83**, 053304 (2012).

[38] K. Schmid, A. Buck, C. M. S. Sears, J. M. Mikhailova, R. Tautz, D. Herrmann, M. Geissler, F. Krausz, and L. Veisz, Density-transition based electron injector for laser driven wakefield accelerators, Phys. Rev. ST Accel. Beams **13**, 091301 (2010).

[39] J. Allison, K. Amako, J. Apostolakis, P. Arce, M. Asai, T. Aso, E. Bagli, A. Bagulya, S. Banerjee, G. Barrand, B. R. Beck, A. G. Bogdanov, D. Brandt, J. M. C. Brown, H. Burkhardt, Ph. Canal, D. Cano-Ott, S. Chauvie, K. Cho, G. A. P. Cirrone *et al.*, Recent developments in geant4, Nucl. Instrum. Methods Phys. Res. Sect. A **835**, 186 (2016).

[40] T. Nakamura, S. V. Bulanov, T. Zh. Esirkepov, and M. Kando, High-Energy Ions from Near-Critical Density Plasmas via Magnetic Vortex Acceleration, Phys. Rev. Lett. **105**, 135002 (2010).

[41] N. Lemos, J. L. Martins, J. M. Dias, K. A. Marsh, A. Pak, and C. Joshi, Forward directed ion acceleration in a lwfa with ionization-induced injection, J. Plasma Phys. **78**, 327 (2012).

[42] S. S. Bulanov, A. Brantov, V. Yu. Bychenkov, V. Chvykov, G. Kalinchenko, T. Matsuoka, P. Rousseau, S. Reed, V. Yanovsky, D. W. Litzenberg, K. Krushelnick, and A. Maksimchuk, Accelerating monoenergetic protons from ultrathin foils by flat-top laser pulses in the directed-coulomb-explosion regime, Phys. Rev. E **78**, 026412 (2008).

[43] J. Huijts, L. Rovige, J. Monzac, I. A. Andriyash, A. Vernier, M. Ouillé, J. Kaur, Z. Cheng, R. Lopez-Martens, and J. Faure, Carrier-envelope phase controlled electron dynamics in a laser-wakefield accelerator, *Optica High-brightness Sources and Light-driven Interactions Congress 2022* (Optica Publishing Group, Washington, DC, 2022), p. HW6B.1.

[44] S. Xu, J. Zhang, N. Tang, S. Wang, W. Lu, and Z. Li, Periodic self-injection of electrons in a few-cycle laser driven oscillating plasma wake, AIP Adv. **10**, 095310 (2020).

[45] A. Sharma, High energy electron and proton acceleration by circularly polarized laser pulse from near critical density hydrogen gas target, Sci. Rep. **8**, 2191 (2018).

[46] V. T. Tikhonchuk, A. A. Andreev, S. G. Bochkarev, and V. Y. Bychenkov, Ion acceleration in short-laser-pulse interaction with solid foils, Plasma Phys. Controlled Fusion **47**, B869 (2005).

[47] A. V. Brantov, V. T. Tikhonchuk, O. Klimo, D. V. Romanov, S. Ter-Avetisyan, M. Schnürer, T. Sokollik, and P. V. Nickles, Quasi-mono-energetic ion acceleration from a homogeneous composite target by an intense laser pulse, Phys. Plasmas **13**, 122705 (2006).

[48] S. C. Wilks, A. B. Langdon, T. E. Cowan, M. Roth, M. Singh, S. Hatchett, M. H. Key, D. Pennington, A. MacKinnon, and R. A. Snavely, Energetic proton generation in ultra-intense laser-solid interactions, Phys. Plasmas **8**, 542 (2001).

[49] P. Mora, Plasma Expansion into a Vacuum, Phys. Rev. Lett. **90**, 185002 (2003).

[50] Zs. Lécz and A. Andreev, Shock wave acceleration of protons in inhomogeneous plasma interacting with ultrashort intense laser pulses, Phys. Plasmas **22**, 043103 (2015).